

Scalable Layered Heterogeneous Hydrogel Fibers with Strain-Induced Crystallization for Tough, Resilient, and Highly Conductive Soft Bioelectronics

Pengle Cao, Yu Wang, Jian Yang, Shichao Niu, Xinglong Pan, Wanheng Lu, Luhong Li, Yiming Xu, Jiabin Cui, Ghim Wei Ho,* and Xiao-Qiao Wang*

The advancement of soft bioelectronics hinges critically on the electromechanical properties of hydrogels. Despite ongoing research into diverse material and structural strategies to enhance these properties, producing hydrogels that are simultaneously tough, resilient, and highly conductive for long-term, dynamic physiological monitoring remains a formidable challenge. Here, a strategy utilizing scalable layered heterogeneous hydrogel fibers (LHHFs) is introduced that enables synergistic electromechanical modulation of hydrogels. High toughness (1.4 MJ m^{-3}) and resilience (over 92% recovery from 200% strain) of LHHFs are achieved through a damage-free toughening mechanism that involves dense long-chain entanglements and reversible strain-induced crystallization of sodium polyacrylate. The unique symmetrical layered structure of LHHFs, featuring distinct electrical and mechanical functional layers, facilitates the mixing of multi-walled carbon nanotubes to significantly enhance electrical conductivity (192.7 S m^{-1}) without compromising toughness and resilience. Furthermore, high-performance LHHF capacitive iontronic strain/pressure sensors and epidermal electrodes are developed, capable of accurately and stably capturing biomechanical and bioelectrical signals from the human body under long-term, dynamic conditions. The LHHF offers a promising route for developing hydrogels with uniquely integrated electromechanical attributes, advancing practical wearable healthcare applications.

1. Introduction

The human body, akin to a soft machine, continually emits highly personalized mechanical, electrical, and biochemical signals that reflect our activities and health conditions.^[1] Emerging soft bioelectronics, particularly for wearable on-skin devices, offer new opportunities for recording those physiological signals non-invasively and in real-time, playing a pivotal role in revolutionizing personalized healthcare.^[2–5] Among various materials, hydrogels are especially advantageous for on-skin bioelectronic applications, owing to their soft and stretchable mechanical properties that match the human body, widely tunable electrical and biological functions, and biocompatible nature.^[6] Therefore, hydrogel-based soft bioelectronics have attracted increasing attention in recent years.^[7] Significant progress has been made in developing on-skin hydrogel electronic devices, providing real-time physiological signals that are closely relevant to human body states. However, the reliability and stability of the sensing signals in a long-term

P. Cao, Y. Wang, J. Yang, X.-Q. Wang
 National Engineering Laboratory for Modern Silk
 College of Textile and Clothing Engineering
 Soochow University
 Suzhou 215123, P. R. China
 E-mail: xqwang@suda.edu.cn
 S. Niu
 Key Laboratory of Bionic Engineering (Ministry of Education)
 Jilin University
 Changchun, Jilin 130022, P. R. China

X. Pan, W. Lu, G. W. Ho
 Department of Electrical and Computer Engineering
 National University of Singapore
 4 Engineering Drive 3, Singapore 117583, Singapore
 E-mail: elehgw@nus.edu.sg

L. Li, Y. Xu
 PPM Institute of Functional Materials
 Poly Plastic Masterbatch (Suzhou) Co., Ltd.
 Suzhou 215144, P. R. China

J. Cui
 State Key Laboratory of Radiation Medicine and Protection
 School for Radiological and Interdisciplinary Sciences (RAD-X) and
 Collaborative Innovation Centre of Radiation Medicine of Jiangsu Higher
 Education
 Soochow University
 Suzhou 215123, P. R. China

 The ORCID identification number(s) for the author(s) of this article can be found under <https://doi.org/10.1002/adma.202409632>

DOI: 10.1002/adma.202409632

integration of these devices with the body still remain unresolved. To achieve this goal, three main requirements need to be met simultaneously. First of all, hydrogels should be tough and stretchable, so as to withstand repeated stretching and deformation (>100% strain) of the on-skin device during dynamic human activities.^[8] Conventional hydrogels are usually fragile,^[9] and their toughness is enhanced by representative strategies, such as interpenetrating networks,^[10] dual-crosslinked networks,^[11] and nanocomposite networks.^[12] Second, the high mechanical resilience of hydrogels is crucial for signal fidelity. Mechanical fatigue of hydrogels will lead to device dysfunctions, such as attenuation or instability of the sensing signals. Therefore, in addition to toughness, enhancing the resilience of hydrogels has also become a research hotspot in recent years.^[13,14] Unfortunately, the widely employed energy dissipation mechanism for toughening hydrogels often creates a trade-off between toughness and resilience. Several newly developed hydrogels, such as slide-ring hydrogel with strain-induced crystallization (SIC),^[15] highly entangled polyacrylamide/polyethylene glycol hydrogel,^[16,17] and polyacrylamide hydrogel with nanochannels of covalent organic frameworks or molecular sieves,^[18] have shown remarkably high toughness and low hysteresis. Nevertheless, the preparation of these hydrogels usually requires careful structural optimization through multistep, time-consuming procedures (ranging from hours to days), and their shaping relies on custom-designed molds. Consequently, these strategies are not applicable to the continuous manufacturing of tough and resilient hydrogel electronic devices. The third requirement is high conductivity. Highly conductive and soft electrodes can enhance electrical communication between tissues and external electronics by decreasing interfacial impedance and improving charge injection capacity for reliable bioelectronic recording,^[19] and facilitate the fabrication of fully soft electronic devices without rigid components (i.e., silicon or metals).^[20] While incorporating electrically conductive nanomaterials or ionic liquids into hydrogels has largely enhanced conductivity, it often compromises desirable biomechanical properties of hydrogels such as softness, resilience, and biocompatibility.^[21–24] To date, fabricating hydrogels and hydrogel bioelectronic devices that are simultaneously tough, resilient, and highly conductive persists to be a daunting challenge, which has hindered the realization of long-term stable, reliable physiological monitoring.

Herein, we propose a strategy using scalable layered heterogeneous hydrogel fibers (LHHFs) to synergistically regulate the electromechanical properties of hydrogels, enabling the manufacture of tough, resilient, and highly conductive soft bioelectronic sensors. Through microchannel-integrated wet spinning and an antisolvent phase separation method, a three-layer gel can be stably extruded and solidified rapidly, enabling continuous spinning of monolithic LHHFs. As illustrated in **Figure 1a**, LHHF has a three-layer, symmetric structure. The middle layer is composed of coiled long-chain sodium polyacrylate (PANa) in highly entangled states, while the two side layers are extended long-chain PANa mixed with multi-walled carbon nanotubes (PANa-MWCNTs). Under continuous stretching, the highly entangled networks of coiled, long-chain PANa undergo deformation, rearrangement, and alignment, accompanied by reversible SIC, thereby toughening the hydrogel while maintaining high resilience. The extended long-chain PANa mixed with MWCNTs

endows LHHFs with electrical conductivity without compromising mechanical resilience, benefiting from the symmetric sandwich structure. Therefore, LHHFs materialize combinational attributes of high toughness, resilience, and conductivity, which are rarely achieved in previous works. LHHFs function effectively as capacitive iontronic strain/pressure sensors, displaying stable signals without decay under 10 000 consecutive cycles of 200% strain or 500 Pa pressure. In addition, LHHFs serve as highly conductive epidermal electrodes, facilitating long-term stable electrocardiogram (ECG) monitoring up to 48 h. We demonstrate wireless multichannel monitoring of full-body physiological signals using LHHFs, including ECG recording, arm and facial motion sensing through electromyography (EMG), to knee and foot motion sensing, which are stable and accurate in long-duration, dynamic scenarios.

2. Results and Discussion

2.1. One-Step, Scalable Fabrication of LHHFs

The process of one-step, continuous spinning of LHHFs is illustrated on the left of **Figure 1a**. By utilizing a custom-designed spinning nozzle with three parallel channels, a PANa hydrogel dope at pH 9.16 as the middle phase, and PANa-MWCNTs hydrogel dopes at pH 13.42 as the two side phases, are simultaneously extruded into a coagulation bath, and the solidified fibers are continuously collected by an electric roller (**Figure S1** and **Movie S1**, Supporting Information). The PANa-based hydrogel dopes exhibit viscoelastic behavior. High viscosity plays a crucial role in enhancing the interface bonding between layered hydrogels (**Figure S2a**, Supporting Information), allowing them to quickly adhere together and maintain layered shapes during dynamic extrusion. The viscosity decreases with increased shear rate, suggesting the shear thinning behavior favorable for extrusion. Rheological measurements show that the storage modulus (G') and loss modulus (G'') of the hydrogel dopes remain almost constant until the oscillation strain reaches $\approx 100\%$, indicating that the hydrogel dopes can withstand relatively large elastic deformation. The gel-to-sol cross-over points of the PANa and PANa-MWCNTs hydrogel dopes are at 671% and 411%, respectively (**Figure S2b**, Supporting Information). **Figure S3** (Supporting Information) shows that an increase in the contents of MWCNTs within the PANa-MWCNTs hydrogel dopes results in enhanced viscosity and modulus. This is ascribed to the high modulus of MWCNTs and their uniform dispersion within the hydrogel dopes. Notably, a composite hydrogel dope containing 70 wt% MWCNTs retains the desired shear-thinning behavior. Furthermore, composite hydrogel fibers with varying MWCNTs concentrations can be produced without a significant alteration in their geometric dimensions (**Figure S4**, Supporting Information). Methanol is used as the antisolvent due to its higher affinity for water than the carboxylate groups in PANa. During the coagulation process, methanol quickly captures water inside the hydrogel dopes and thus drives a phase separation. Aggregation and conformational changes of the polyelectrolyte chains occur, and the 3D network structure gradually collapses. **Movie S2** (Supporting Information) shows the phase separation process of LHHFs in methanol. Afterward, the dehydrated LHHFs are exposed to the ambient environment to spontaneously capture moisture from the

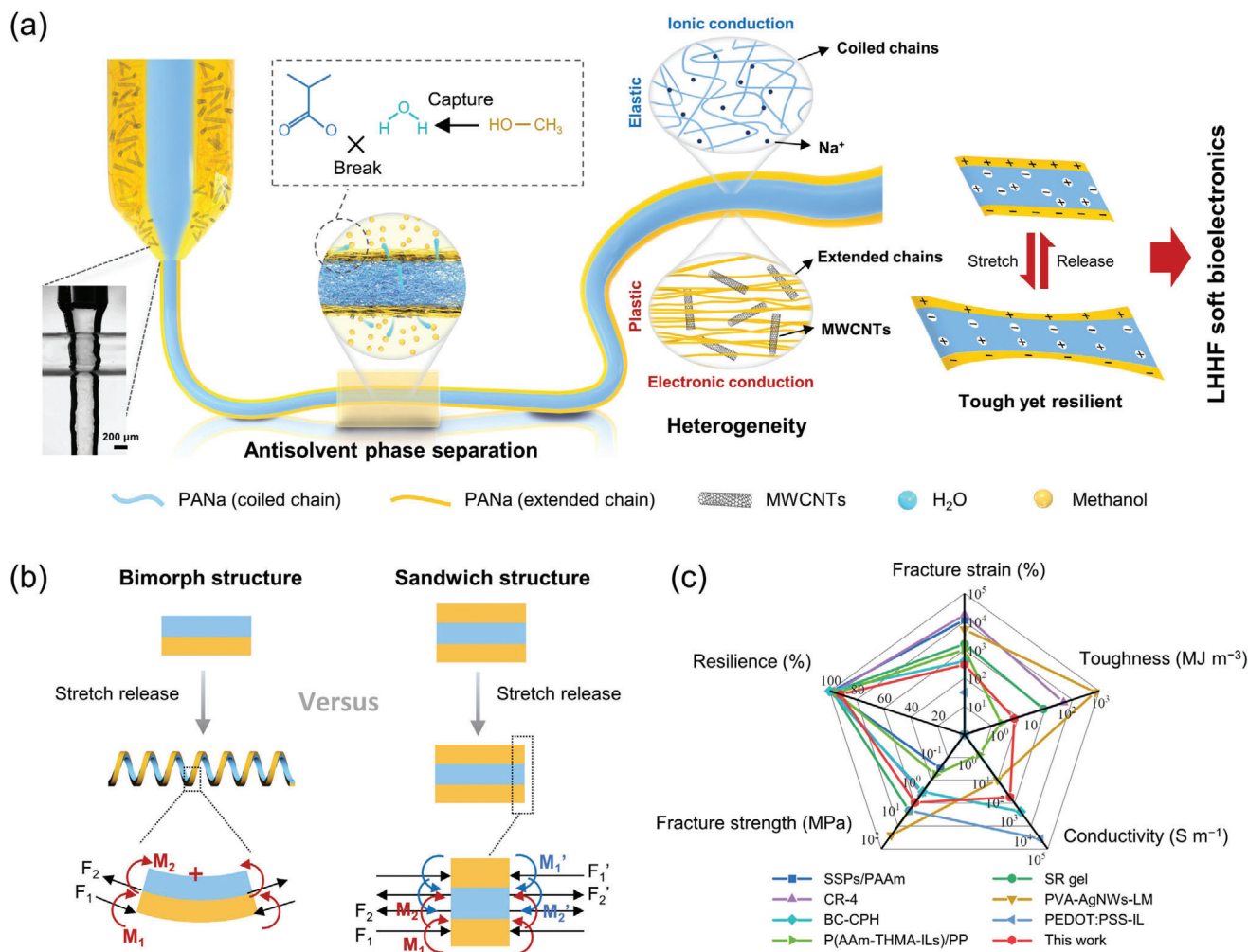


Figure 1. Fabrication and microstructures of LHHFs. a) Schematic illustration for the fabrication of LHHFs toward soft bioelectronic applications. b) Schematic illustration for the structure of the E-layer and M-layer, and the shape change of different layered structures in response to a stretching-releasing process. c) Radar chart for comprehensive electromechanical performances of various representative hydrogels including the SSPs/PAAm,^[13] the SR gel,^[15] the CR-4,^[18] the PVA-AgNWs-LM,^[27] the BC-CPH,^[28] the PEDOT:PSS-IL,^[21] the P(AAm-THMA-ILs)/PP,^[29] and the LHHF hydrogel developed in this work.

atmosphere (65% humidity), and the stabilized LHHFs are soft and stretchable. In LHHFs with heterogeneous hydrogel layers, the middle layer of PANa hydrogel has a highly entangled network of coiled PANa chains, which is responsible for constructing a mechanically elastic layer (M-layer), and has ionic conductivity owing to its polyelectrolyte nature. The two side layers are composite hydrogels consisting of MWCNTs and extended PANa chains (E-layer), which have high electrical conductivity and plastic deformation characteristics due to the high content of MWCNTs (50 wt%). In a bimorph strip, a strain mismatch between two layers produces bending moments and thus bending/coiling deformation (Figure 1b, left).^[25,26] Accordingly, a straight bimorph hydrogel fiber consisting of an M-layer and an E-layer will transform into a helical fiber under a stretching-releasing process (Figure 1b, right). In contrast, in LHHFs with the symmetric sandwich structure subjected to stretching-releasing, negative and positive bending moments produced respectively on the upper and lower interfaces be-

tween the M-layer and E-layers are equal. As a result, LHHFs are free from structural failure induced by stretching and are stretchable and recoverable (See more details in Figure S5, Supporting Information). Although tough hydrogels, tough and resilient hydrogels, and highly conductive hydrogels have been fabricated, fabricating hydrogels that are simultaneously tough, resilient, and highly conductive is extremely difficult (Figure 1c). Leveraging the symmetric sandwich structure and heterogeneous properties of the M-layer and E-layer, LHHFs exhibit uniquely combined electromechanical attributes of high toughness, resilience, and conductivity, superior to most existing hydrogels (Table S1, Supporting Information).

2.2. Electromechanical Properties Modulation of LHHFs

As shown on the left of Figure 2a, the proposed microchannel-integrated wet spinning technology demonstrates the feasibility

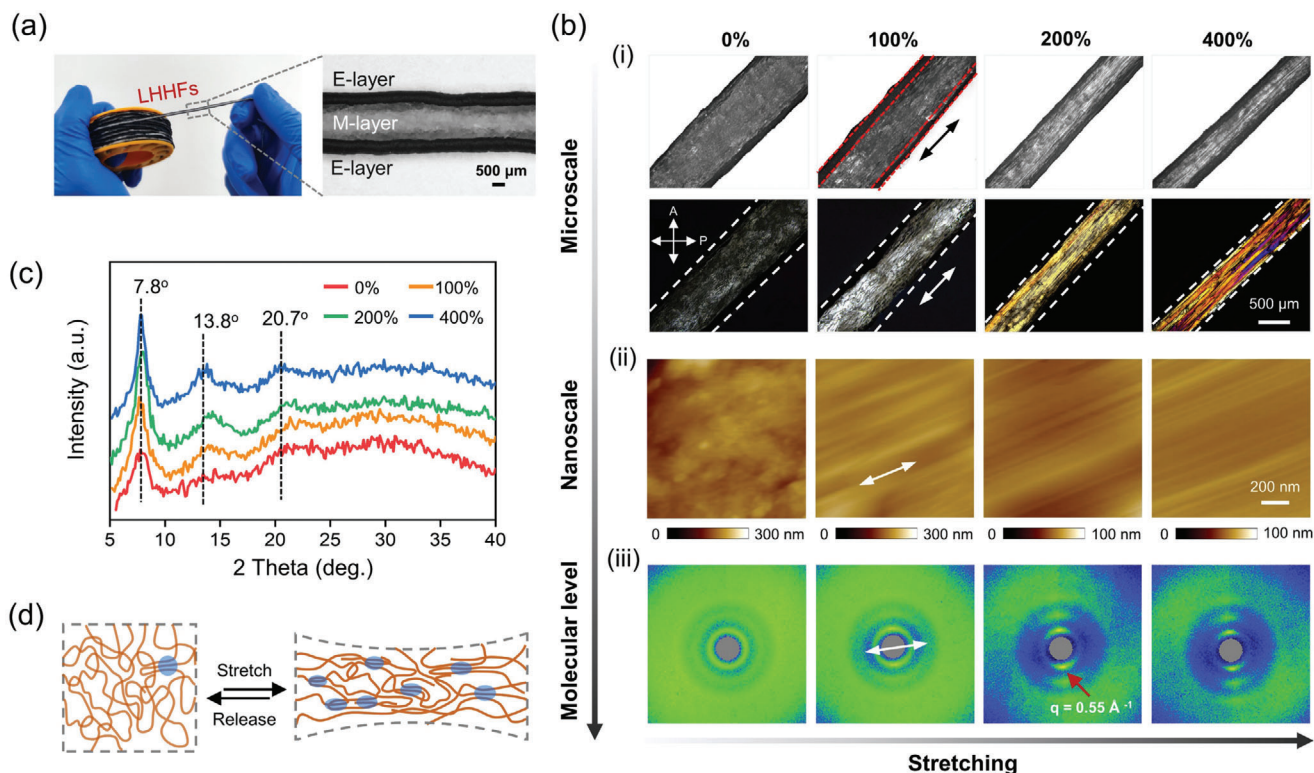


Figure 2. Multiscale structural characterization of LHHFs under stretching. a) A photograph of several meters of LHHFs wrapped around a spool (left) and an optical microscope image of an LHHF along the length direction (right). b) (i) Optical microscope images of LHHFs at different strains captured under visible light (top) and polarized light (bottom). (ii) AFM images and (iii) WAXS patterns of the middle layer PANa hydrogel under different strains. The arrows indicate the stretching directions. c) WAXS profiles of the PANa hydrogel at different strains. d) Schematic illustration of the PANa hydrogel network under stretching/releasing.

of digitalized manufacturing of continuous meter-scale LHHFs. From the optical microscope image, we can observe that the LHHF maintains good structural integrity and continuity along its length direction (Figure 2a, right). In addition, the cross-sectional scanning electron microscope (SEM) image shows that the E-layers on the two sides of the LHHF tightly adhere to the middle M-layer, and the M-layer reveals a microporous structure (Figure S6a, Supporting Information). The surface of the M-layer is uniform (Figure S6b, left, Supporting Information) owing to the high homogeneity of the highly entangled PANa networks. Well-dispersed MWCNTs can be observed on the surface of the E-layer, which provides a continuous network that gives LHHFs high conductivity (Figure S6b, right, Supporting Information). Tough yet resilient hydrogels feature damage-free toughening when stretched and fully reversible structural recovery when released. The multiscale structural evolution of LHHFs under stretching/releasing was studied. The optical microscope images under visible light show that the layered hydrogels in LHHFs maintain robust interfacial bonding without delamination under stretching (top of Figure 2b(i)). The corresponding optical microscope images under polarized light present that the middle layer PANa hydrogel yields vivid interference color changes as the LHHF is stretched. Initially, the PANa hydrogel appears invisibly white, transitioning to bright white, yellow, and pink at 100%, 200%, and 400% strains, respectively. This sequential change matches the order of colors in the Michel-Levy color

chart as birefringence increases (bottom of Figure 2b(ii)),^[30] indicating gradual alignment of polymer chains along the stretching direction. Moreover, this interference color change was reversible upon stress removal, with the LHHF rapidly returning to its original shape (Figure S7 and Movie S3, Supporting Information), suggesting no significant structural damage occurred in the PANa hydrogel during the stretching/releasing process. SEM images in Figure S8 (Supporting Information) show that microscale structural orientation in the PANa hydrogel happens during stretching. Atomic force microscopy (AFM) captures nanoscale structures of the PANa hydrogel at different strains (Figure 2b(ii); Figure S9, Supporting Information). Small polymer nanoclusters are observed in the PANa hydrogel at the initial state, attributed to random entanglements of coiled polymer chains. With increasing strain, the polymer chains gradually extend and aggregate during the stretching process, resulting in more pronounced nanofiber structures along the stretching direction. Furthermore, we used wide-angle X-ray scattering (WAXS) measurements to determine the physical interactions of PANa macromolecular chains during stretching (Figure 2b(iii)). Before stretching, a nearly homogenous diffraction ring is observed in the WAXS pattern owing to the isotropic structure of the PANa hydrogel. Stretching promotes molecular orientation, yielding a strongly angle-dependent diffraction pattern with high-intensity arc areas perpendicular to the stretching direction at 100%, 200%, and 400% strains. The WAXS profiles

in Figure 2c reveal three diffraction peaks at $2\theta = 7.8^\circ$, 13.8° , and 20.7° , indicating the presence of crystalline domains in the PANa hydrogel. The peaks at $2\theta = 7.8^\circ$ and 13.8° respectively correspond to (010) and (001) reflections of PANa crystalline with orthorhombic unit cells.^[31] The diffraction peaks increase continuously with strain, indicating that mechanical stress induces the formation of crystalline domains. In addition, the integrated intensity ($2\theta = 7.8^\circ$) scans as a function of azimuthal angle are shown in Figure S10a (Supporting Information), which are utilized to calculate macromolecule orientation parameters at different strains.^[32] The orientation factor (*f*) of the unstretched sample is approximately zero, implying random orientation of the polymer chains. As the applied strain increases from 100% to 400%, the newly formed crystalline domains are oriented along the stretching direction, and the *f*-value rises from ≈ 0.64 to 0.86 (Figure S10b, Supporting Information), signifying a high degree of polymer chain orientation. The crystallinity of the PANa hydrogel at 400% strain is 35%, which is 26% greater than that of the unstretched sample. Based on the aforementioned findings, we conclude that the middle layer PANa hydrogel with reversible SIC is essential for toughening LHHFs while maintaining high resilience. The initial PANa hydrogel is an isotropic, highly entangled network of coiled long chains. A large number of physical entanglements serve as crosslinking points that maintain the structural integrity and stability of the hydrogel, and a low crystallinity exists. Under stretching, the tension in a PANa chain transmits along the length direction of the chain and to many other chains through entanglements, leading to high stretchability and toughness. With increased strain, the extended chains highly orientate along the stretching direction, aggregate together, and form aligned crystalline domains. These domains hinder the sliding or breakage of polymer chains, thus further toughening the hydrogel. Upon release, the temporarily aligned PANa chains revert to a random configuration driven by entropy, enabling high resilience (Figure 2d). Additionally, the incorporation of MWCNTs into the PANa hydrogel results in a reduction of its initial crystallization (See more details in Figure S11, Supporting Information). Furthermore, the continuous tension transitions among the PANa chains are effectively disabled under mechanical stretching. Consequently, strain-induced reinforcement of crystallization is not observed in the PANa-MWCNTs hydrogel (Figure S12, Supporting Information). Therefore, this unique PANa hydrogel system, characterized by dense long-chain entanglements and reversible SIC, is expected to confer high toughness and resilience to LHHFs.

In addition to being tough and resilient to achieve mechanical durability and stability for long-term usage, the high conductivity of hydrogels is highly desirable to reduce reliance on rigid silicon or metal-based conductive elements and enhance electrical communication between tissues and all-soft hydrogel sensors. Herein, by optimizing the structures of the middle M-layer and the two side E-layers in LHHFs, high toughness, resilience, and conductivity can be simultaneously achieved. We first performed uniaxial tensile tests to measure the mechanical properties of the M-layer PANa hydrogel fiber. PANa fibers with different sizes are highly stretchable and can be extended over 5 times their original length without breaking (Figure S13a, Supporting Information). The fracture strength and toughness are over 0.1 MPa and 0.4 MJ m^{-3} , respectively. Cycled tensile tests

of PANa fibers at 200% strain show very small residual strain ($<1.8\%$) and hysteresis ($<7.6\%$) (Figure S13b, Supporting Information). These high toughness and resilience are attributed to the long-chain entanglements of coiled PANa and reversible SIC, as discussed earlier. The PANa hydrogel mixed with MWCNTs is expected to endow LHHFs with high electrical conductivity.^[33] As shown in Figure 3a, the PANa hydrogel has an ionic conductivity of $\approx 2.1 \text{ S m}^{-1}$, while the electronic conductivity of the PANa hydrogel mixed with 70 wt% MWCNTs reaches $\approx 1550.1 \text{ S m}^{-1}$. However, the mixing of MWCNTs largely sacrifices the stretchability and resilience of the PANa hydrogel. The fracture strain of the PANa-MWCNTs (70 wt%) hydrogel is $\approx 280.2\%$, with a residual strain under a cycled 100% strain test reaching $\approx 44.4\%$ (Figure 3b and Figure S14, Supporting Information). In the design of LHHFs, PANa hydrogel mixed with 50 wt% MWCNTs is chosen as the E-layers, offering a conductivity of $\approx 844.2 \text{ S m}^{-1}$ and fracture strain of $\approx 460.5\%$. Furthermore, we optimized the electromechanical properties of LHHFs by varying the width of the E-layer and the thickness of the M-layer (Figure S15, Supporting Information). The stress-strain curves of LHHFs in Figure 3c show that the E-layer on one side of an LHHF breaks first, leading to a decrease in the fracture strength, but the LHHF can still be further stretched until complete fracture. With a fixed width of the M-layer, increasing the width of the E-layer enhances the fracture strength while decreasing the fracture strain (Figure S16, Supporting Information). Furthermore, maintaining a constant width for both the E-layer and the M-layer, an increase in the thickness of the M-layer, which consequently enhances the fiber's cross-sectional area, leads to a decrease in both fracture strength and fracture strain (Figure S17a, Supporting Information). The electrical conductivity also significantly decreases as the thickness of the M-layer increases (Figure S17b, Supporting Information). Taken together, LHHFs exhibit widely tunable electromechanical properties, including conductivity ($21.6\text{--}298.5 \text{ S m}^{-1}$), fracture strain ($237.2\text{--}440.1\%$), and toughness ($0.2\text{--}4.5 \text{ MJ m}^{-3}$) (Figure 3d). The optimized LHHF exhibits a conductivity of 192.7 S m^{-1} , a toughness of 1.4 MJ m^{-3} , and a fracture strain of 341.7% , which was used as a representative sample for further tests (See more details in Figure S18, Supporting Information). Meanwhile, the LHHF exhibits negligible differences in its stress-strain behavior between room temperature ($\approx 25^\circ \text{C}$) and human body temperature ($\approx 37^\circ \text{C}$) (Figure S19, Supporting Information). Figure S20 (Supporting Information) presents the relatively constant electrical conductivity of the LHHFs, which were prepared under identical conditions across different batches.

Although PANa-MWCNTs hydrogel fibers undergo plastic deformation under stretching, the optimized LHHF with symmetric E-layers on both sides of the M-layer demonstrate high mechanical resilience. Under a cycled tensile strain of 25% to 200%, LHHFs display low hysteresis loops (Figure 3e). During tensile tests at 200% strain for 250 consecutive cycles, LHHF displays high resilience (92%) after the first cycle and increases to 96% after the fifth cycle, which remains almost constant during the subsequent cycles (Figure S21, Supporting Information). At different stretching rates, LHHFs still exhibit high resilience with minimal residual strains (Figure S22, Supporting Information). Figure 3f and Movie S4 (Supporting Information) illustrate the rapid recovery of PANa fibers upon release from 250% strain, while PANa-MWCNTs fiber exhibits plastic deformation post-release.

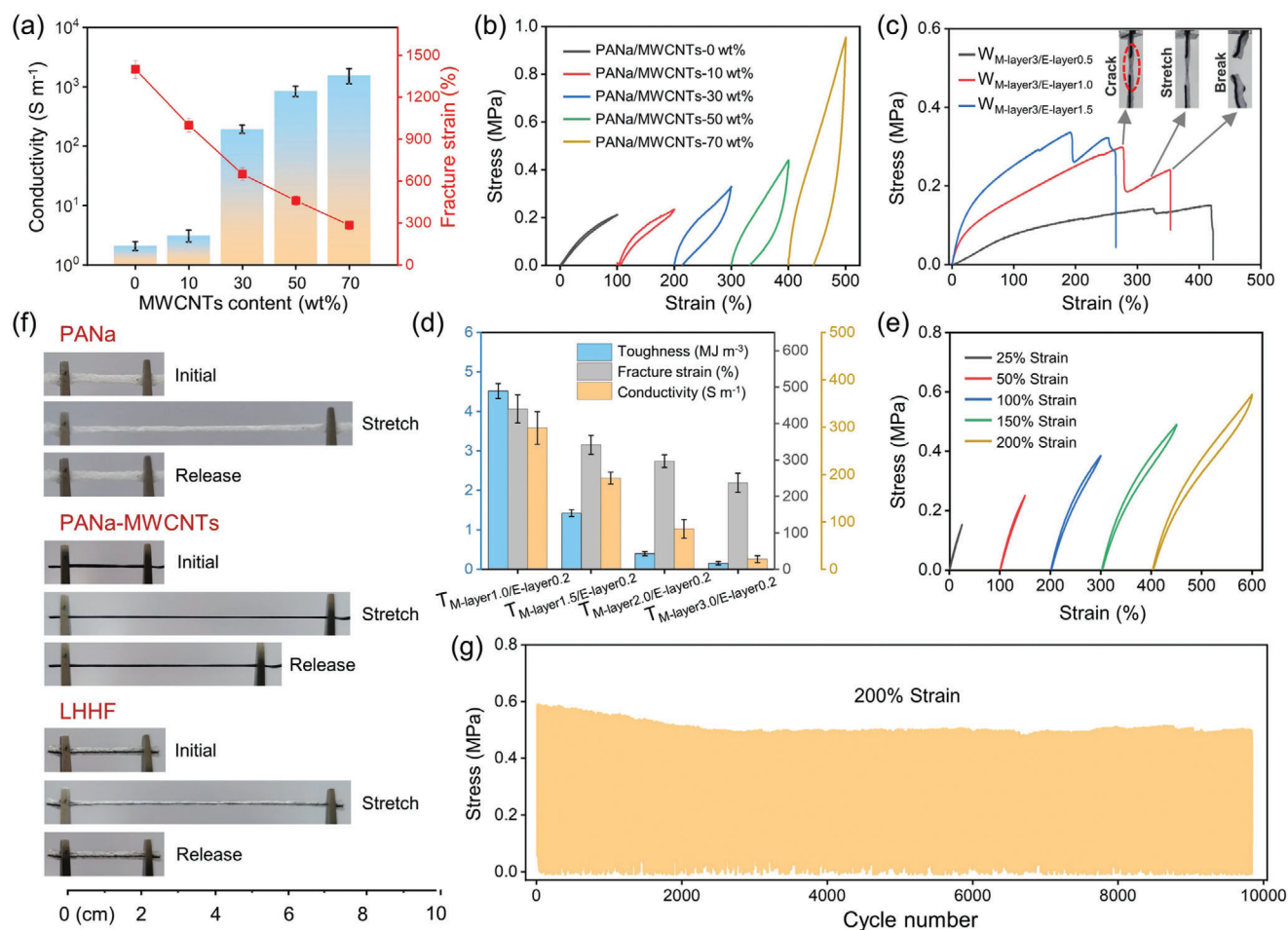


Figure 3. Electromechanical performances of LHHFs. a) Electrical conductivity and fracture strain of PANa hydrogel fibers with different MWCNTs contents. b) Stress–strain profiles of PANa hydrogel fibers with different MWCNTs contents subjected to a loading–unloading cycle of 100% strain. The curves are horizontally offset for clarity. c) Stress–strain curves of LHHFs with different $W_{E-layer}$ (scale: mm). Insets show the cracking, stretching, and breaking of an LHHF during a stress–strain testing. d) Toughness, fracture strain, and conductivity of LHHFs with different $T_{M-layer}$ (scale: mm). e) Stress–strain profiles of the optimized LHHF subjected to a loading–unloading cycle at different strains. The curves are horizontally offset for clarity. f) Photographs of a PANa hydrogel fiber, a PANa-MWCNTs hydrogel fiber, and an LHHF in the initial, 250% strain loaded, and unloaded states. g) Mechanical strength of the LHHF at 200% strain during 9800 loading–unloading cycles.

Notably, all of the LHHFs exhibit fast resilience comparable to that of the elastic PANa fiber, without observable permanent deformation. Additionally, the fatigue resistance of LHHF was evaluated by subjecting it to 9800 consecutive cycles of 200% strain. As shown in Figure 3g, the tensile strength declines marginally in the first ≈ 3000 cycles and stabilizes thereafter for thousands of cycles. Compression tests on LHHFs validate stable compressive strength under 900 consecutive cycles of 50% compressive strain, with no structural collapse over a prolonged period (Figure S23, Supporting Information). These results underscore that the optimized LHHF exhibits high toughness, resilience, and conductivity, making it suitable for long-term soft bioelectronic sensing applications.

The LHHF consists of two symmetrical electrodes (E-layers) and an ionic dielectric (M-layer) sandwiched between them. This structural feature, combined with its remarkable toughness and resilience, makes it a capacitive iontronic strain/pressure sensor.^[34,35] An equivalent circuit diagram of the iontronic

sensor is illustrated in Figure 4a, in which electrical double-layer capacitances (C_{EDL}) at the ionic conductor/electronic conductor interfaces can be modeled as two variable capacitors connected through a variable resistor of the M-layer.^[36,37] Besides, additional capacitive change (C_{PE}) results from the electric coupling of the two electrode surfaces in parallel, similar to the classic parallel-plate capacitance, whose magnitude is typically marginal compared to that of the EDL capacitance. Therefore, the key performance of the iontronic strain/pressure sensor is governed by the deformation-controlled EDL capacitances. Then, we investigated the effect of M-layer thickness on the sensitivity (gauge factor GF, defined as the relative capacitance change $\Delta C/C_0$ over the applied strain ϵ) of the iontronic strain sensor. Cross-sectional SEM images depict a greater abundance of microporous structures in the LHHFs with increased M-layer thickness, which are characterized by lower initial capacitances (Figure S24a, Supporting Information). Moreover, the strain sensitivity is substantially enhanced (See more details in Figure S24b, Supporting

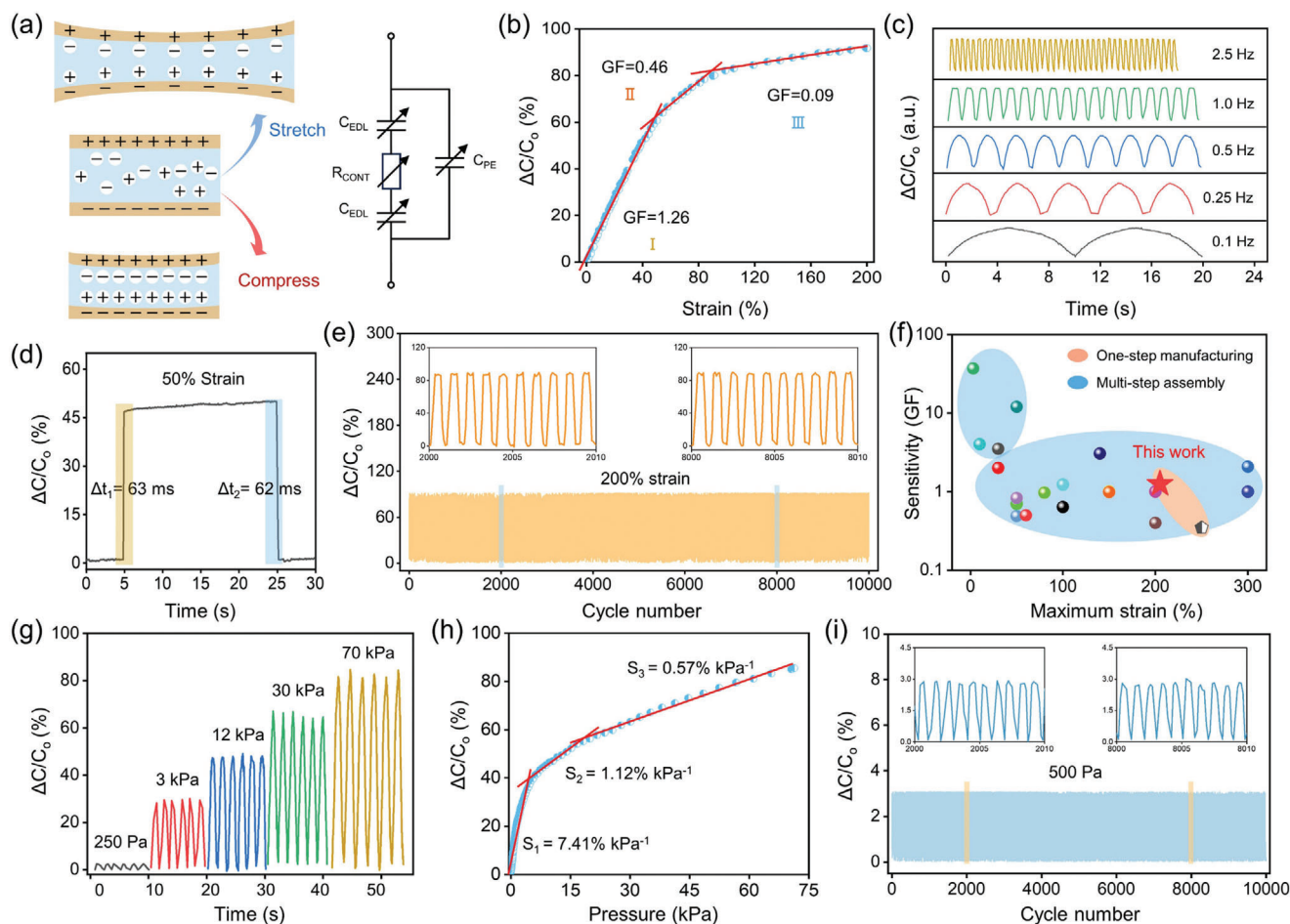


Figure 4. LHHF capacitive iontronic strain/pressure sensors. a) Schematic for the strain/pressure sensing mechanism of the LHHF capacitive iontronic sensor and the equivalent circuit diagram. b) Relative capacitance changes over 0–200% strain and the corresponding GF of the LHHF strain sensor. c) Relative capacitance changes of the LHHF sensor at different stretch frequencies (50% strain). d) Response and recovery time of the LHHF strain sensor during a loading-unloading process of 50% strain. e) Relative capacitance changes of the LHHF strain sensor during 10 000 loading-unloading cycles of 200% strain. f) Comparison of the LHHF capacitive iontronic strain sensor with other reported capacitive strain sensors in terms of sensitivity and maximum strain. The data are summarized in Table S1 (Supporting Information). g) Time-dependent relative capacitance variations of the LHHF sensor with different applied pressure. h) Relative capacitance changes as a function of applied pressure. i) Relative capacitance changes of the LHHF sensor during 10 000 loading-unloading cycles at a low pressure of 500 Pa.

Information). Engineering microporous structures within the ionic polymer matrix to achieve a low dielectric constant is a typical strategy to reduce the initial capacitance, thereby enhancing the relative capacitance change.^[38] Additionally, the effective dielectric constant increases as the micropores gradually shrink under stretching or pressure, leading to an additional increase in ΔC . The LHHF with a microporous M-layer demonstrates a pronounced nonlinear sensitivity within the 200% strain range. Gradual shrinkage of the micropores in the low strain range results in an increase in ΔC , which diminishes gradually as strain increases. Furthermore, the electrical resistance of the LHHF increases substantially in the higher strain range (Figure S25, Supporting Information), which may have caused a decrease in the unit area capacitance, leading to a reduction in ΔC .^[39] These two adverse factors could result in high sensitivity at low strains and a subsequent decline in sensitivity at higher strains. The LHHF iontronic strain sensor reliably detects strain within the range of 5–200%, as shown in Figure S26a (Supporting Informa-

tion). The relationship between the relative capacitance changes and tensile strain is depicted in Figure 4b, which is fitted with three linear equations. The sensitivity reaches 1.26 within 50% strain. Additionally, relative capacitance changes exhibit stability in both slow-adaptive mode and high-frequency dynamic motion modes (Figure S26b, Supporting Information). Figure 4c shows consistent capacitive changes of $\approx 60\%$ in response to 50% strain in the frequency range of 0.1–2.5 Hz. Notably, the sensor demonstrates a relatively fast response time of 63 ms and recovery time of 62 ms at 50% strain with no electrical hysteresis (Figure 4d), which is similar to that of the human skin (50–100 ms).^[40] To assess durability and stability of the iontronic strain sensors, 10000 consecutive cycles of 200% strain are monitored, revealing highly reproducible signals without significant baseline drift (Figure 4e and Figure S27, Supporting Information).

The fabrication of capacitive strain sensors mostly relies on multistep manual assembly, owing to the requirement of two electrode layers and a dielectric layer with different material

compositions. An exception is the capacitive soft strain sensor (CS3) fibers via the specially designed multicore-shell printing approach reported by Lewis et al.^[41] In comparison, the LHHF capacitive strain sensors can be mass-produced by the microchannel-integrated industrial wet spinning method, and this rapid prototyping technique may open new avenues for device innovation and performance breakthroughs. When evaluating strain sensors, sensitivity, and strain detection range are important performance metrics. As summarized in Figure 4f, compared to previously reported capacitive strain sensors, our one-step manufactured LHHF sensor has a relatively high sensitivity of 1.26 (< 50% strain), and a remarkably broad working range of 200% strain (Table S2, Supporting Information of a more detailed comparison). Additionally, pressure-induced capacitance changes in the LHHF iontronic sensor are evaluated (Figure 4g), and the relationship between the relative capacitance change and pressure is depicted in Figure 4h. While the sensitivity (S , defined as the $\Delta C/C_0$ over the applied pressure P) is relatively modest, the capacitance response to specific pressures remains stable, independent of compression rates (Figure S28a, Supporting Information), which benefits from high mechanical resilience of the LHHF. Figure S28b (Supporting Information) shows that the sensor has high response/recovery speeds (239/255 ms), and the relative capacitance changes under 30 kPa pressure for 20 s are constant at $\approx 60\%$ without drift. Moreover, under 10 000 consecutive compression cycles at a subtle pressure of 500 Pa, the capacitance changes are highly repeatable and stable (Figure 4i). Taken together, the one-step manufactured LHHF iontronic sensors feature high accuracy, stability, and durability for long-term and repetitive strain/pressure sensing, making them suitable for monitoring human daily activities.

2.3. LHHF-Based Soft Bioelectronic Sensors

LHHFs, benefiting from their softness, stretchability, and high conductivity, can function as epidermal electrodes to electrically interface with the skin and capture biopotentials. ECG signals are essential in assessing various aspects of heart health, including normal cardiac function, the impact of physical activity on the heart, and the detection of functional abnormalities such as arrhythmias.^[42] To assess the biocompatibility of LHHFs for direct skin applications, *in vivo* studies were conducted on both mouse and human skin (Figures S29 and S30, Supporting Information).^[43,44] The findings demonstrate that the LHHF, akin to the commercial hypoallergenic Ag/AgCl electrode, did not induce significant irritation (i.e., no evidence of edema or erythema) over 72-h experiments, suggesting that our LHHFs are suitable for skin use. To record ECG signals, two LHHF electrodes as working electrodes are symmetrically patched on the left and right chests of a volunteer, while another LHHF electrode serves as the grounding electrode attached to the left abdomen, as shown in Figure 5a. After wetting the skin with a small amount of water, the LHHF electrode can adhere well to the skin, as shown in Figure 5b. A simplified equivalent circuit model describes the LHHF electrode interfacing with the corneous, epidermis, and subcutaneous dermis layers (Figure 5c).^[45] Interfacial impedance analysis between the electrodes and skin at the physiologically relevant frequency of 1–10⁴ Hz was conducted

on the human forearm. The LHHF electrode adheres well on the skin, shows comparable impedance to that of the commercial Ag/AgCl gel electrode, and is slightly lower in the range of 1–100 Hz (Figure S31, Supporting Information). The high conductivity of the LHHF electrode ensures efficient electrical signal transmission, while its stretchability and soft compliance enable its conformal contact with the skin during exercise, ensuring accurate measurements with reduced motion artifacts. As shown in Figure 5d, the LHHF electrodes collect high-quality ECG signals with clear PQRST waveforms, comparable to those obtained with commercial gel electrodes. The RR interval, representing the time between two consecutive R peaks, is calculated to be 780 ms, corresponding to an estimation of a heart rate of 77 bpm. Notably, unlike commercial electrodes that suffer from volatilization of the liquid in the gel electrolyte during long-term usage, the LHHF electrodes are hygroscopic and can self-retain moisture inside the gel network (water content of ≈ 43 wt%). In the long run of continuous monitoring for 48 h, stable ECG signals could be collected by the LHHF electrodes (Figure 5e). The sensitivity, defined as the relative voltage ratio of the measured T peak to R peak in a PQRST waveform (T/R value), evaluates the quality of ECG signals.^[46,47] A higher T/R value indicates a higher accuracy of ECG signals. Figure 5f shows that T/R values of the ECG signals collected during 48 h monitoring maintained at ≈ 0.39 , higher than that of the commercial Ag/AgCl gel electrode (≈ 0.26) measured in this work.

The electrophysiological signals of muscles are highly correlated with human movements. The compliance and low electrical contact impedance of LHHF electrodes make them ideal for monitoring dynamic muscle movements.^[48] As shown in Figure S32 (Supporting Information), two LHHF electrodes were placed on the inner side of the volunteer's left forearm to detect the action potentials generated by muscles, while another electrode at the elbow works as the reference electrode. The LHHF electrodes successfully detect distinguishable low-amplitude EMG signals generated by different finger flexion/extension movements (Figure 5g; Movie S5, Supporting Information). Figure 5h,i respectively shows the EMG signals produced by the biceps muscles of the arms when lifting a dumbbell of different weights and grasping an object at different speeds. It is evident that the greater the force generated by the muscles or the faster their swinging speed, the higher the level of the EMG signals. Additionally, the high sensitivity of LHHF electrodes enables the identification of subtle differences in muscle movements. For instance, when using a dual-channel EMG detection device, LHHF electrodes simultaneously record muscle movements induced by arm flexion/extension and tooth occlusion movements with distinguishable voltage signals (Figure S33, Supporting Information).

2.4. LHHF-Based Multichannel Sensing Platform for Full-Body Physiological Monitoring

LHHF-based multichannel sensing platform was designed for wireless, long-term, and dynamic physiological monitoring. Figure 6a schematically depicts the multichannel wireless system, in which LHHF electrodes deployed on the forearm and cheek detect the arm and facial motion-related muscle

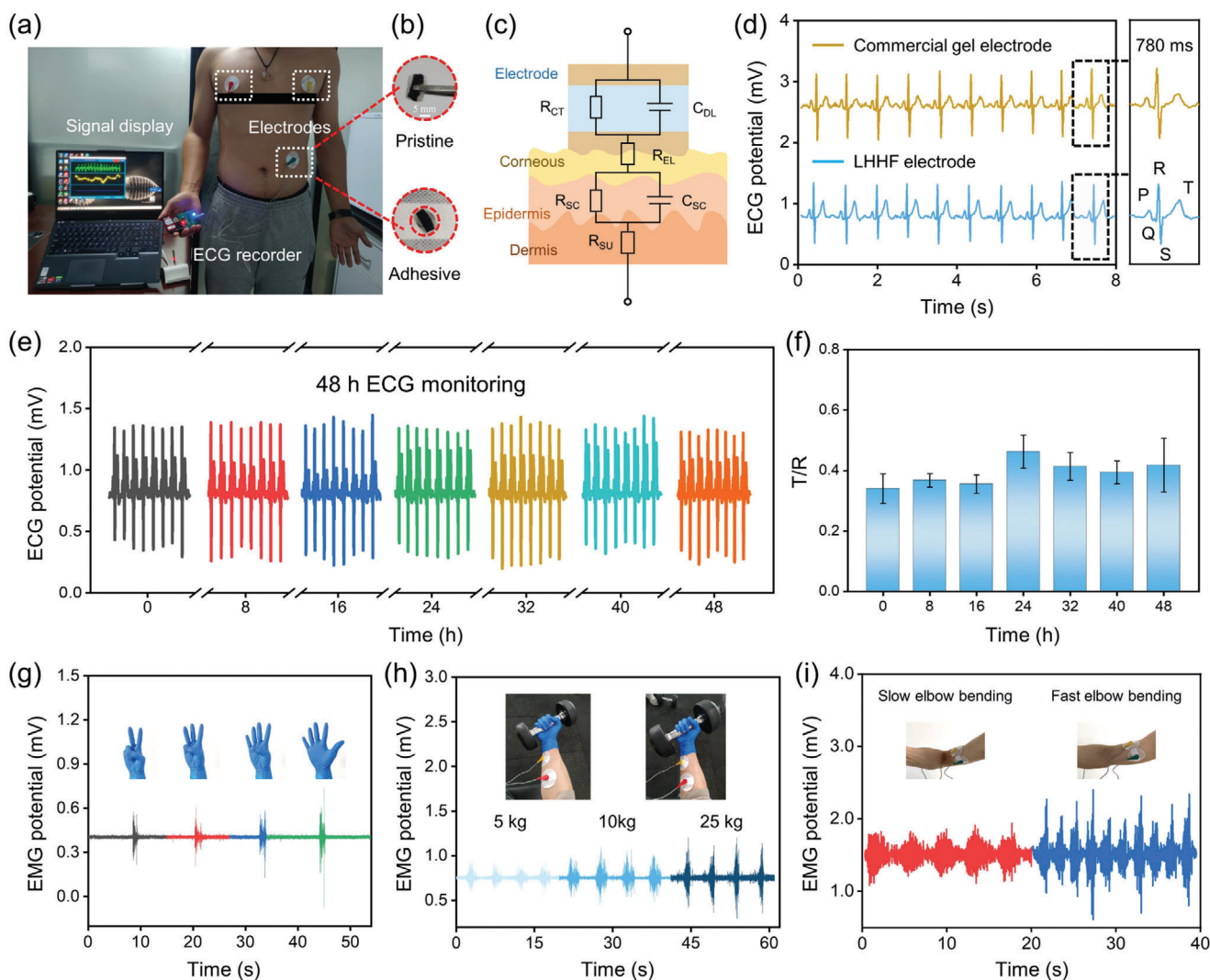


Figure 5. LHHF electrodes for epidermal electrophysiology detection. a) Mounting positions of LHHF electrodes for ECG measurement. b) Photographs of the pristine (top) and adhesive LHHF electrode (bottom). c) Schematic of the equivalent circuit model used for monitoring ECG signals. d) ECG signals recorded by the LHHF electrodes and commercial Ag/AgCl gel electrodes. Characteristic P, Q, R, S, and T waves are clearly identified. e) ECG signals were collected by the LHHF electrodes during 48 h monitoring. f) T/R values of the ECG signals during 48 h monitoring. g) EMG signals of the forearm are generated from different gestures. h) EMG signals of the forearm are generated from different gripping forces. i) EMG signals of the bicipital muscle generated from different gripping speeds.

electrophysiological signals via the EMG module (Channel A), LHHF electrodes attached on the chest collect ECG signals via the channel B, and LHHF iontronic capacitive sensors in the channel C monitor the knee and foot motion related gaits. All sensing signals are simultaneously collected by the sensors, wirelessly transmitted via Bluetooth modules, and displayed on a PC or smartphone for further diagnostic analysis (Figure 6b). Figure 6c–e and Movie S6 (Supporting Information) show a volunteer wearing the LHHF-based sensing platform with LHHF electrodes and LHHF iontronic capacitive sensors placed at desired positions, displaying the EMG and ECG signals on a PC, and recording capacitance signals on a smartphone. As shown in Figure 6f, during walking and jogging, the corresponding ECG, EMG, and capacitance change signals are distinguishable and stable, without baseline drift or peak loss during each movement. The sensing signals

in each channel are highly consistent throughout the 10-min duration at the same walking speed (Figure 6g). Additionally, the LHHF electrodes are capable of accurately recording ECG signals under different states, indicating an increase in the heart rate after exercise (Figure 6h). The LHHF electrodes in Channel A demonstrate high reversibility and stability in multiple cycles of tooth occlusion and arm bending/releasing motion, with negligible electromechanical hysteresis. Moreover, these two types of motions can be differentiated by the intensity of the EMG signal or the change in capacitance when deploying the LHHF iontronic capacitive sensors, as shown in Figure 6i. Besides, LHHF iontronic capacitive sensors in channel C are accurate enough to generate reproducible capacitance changes to reflect the bending angles of the knee and the strength of the footsteps (Figure 6j). In general, the LHHF-based multichannel sensing platform

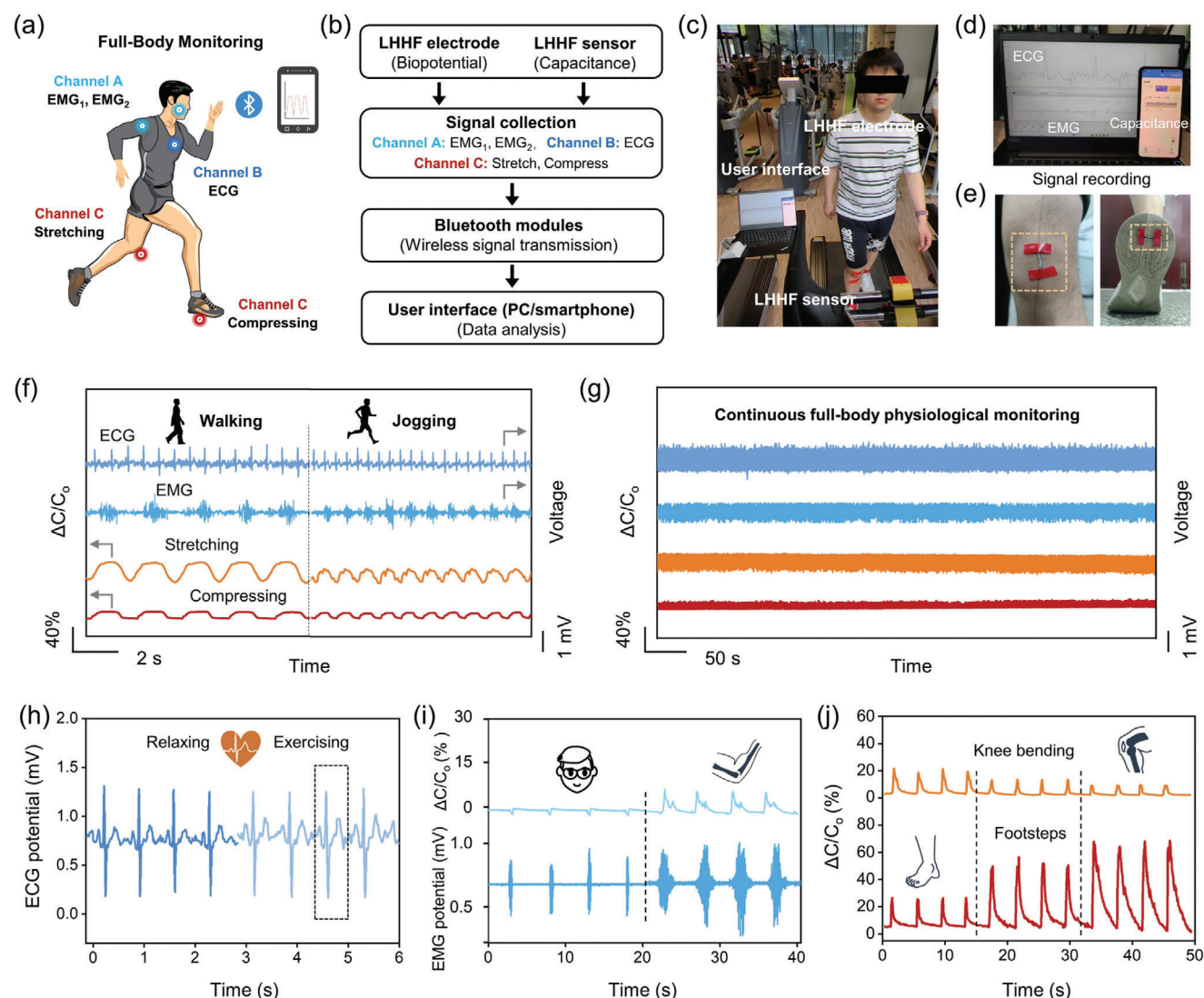


Figure 6. LHHF-based multichannel sensing platform for wireless full-body physiological monitoring. a) Schematic and b) workflow diagram for the LHHF-based multichannel sensing platform. c) A photograph of a volunteer wearing the multichannel sensing platform. d) The real-time sensing signals collected by the sensing platform. e) Photographs of the LHHF iontronic capacitive sensors attached to the knee and sole. (f) The ECG, EMG, and capacitance change signals recorded for a volunteer during continual walking and running. (g) Long-term continuous recording of ECG, EMG, and capacitance change signals. h) ECG signals recorded in channel B before and after exercise. i) EMG recorded in channel C and capacitance signals generated by tooth occlusion and arm bending. j) Relative capacitance changes recorded in channel C in response to different knee bending states and footsteps.

proves to be soft and compliant with the human body, mechanically robust to endure repetitive mechanical loads and provide stable biomechanical and bioelectrical signals under various conditions.

3. Conclusion

We have established a new strategy of LHHFs for developing tough, resilient, and highly conductive soft bioelectronic sensors. The LHHFs feature a three-layer, symmetric layered structure comprising a PANa hydrogel middle layer and PANa-MWCNTs hydrogel two side layers, that can be one-step, mass-produced by a microchannel-integrated wet spinning combined with an

antisolvent phase separation method. Optimized LHHFs simultaneously exhibit high toughness (1.4 MJ m^{-3}) and resilience ($>92\%$ recovery from 200% strain), which is attributed to the damage-free toughening mechanism involving dense long-chain entanglements and reversible SIC of the PANa hydrogel. The unique symmetrical layered structure with separated electrical and mechanical functional layers allows MWCNTs to be mixed to enhance the conductivity of LHHFs without compromising the toughness and resilience, and the resulting LHHF exhibits an exceptional conductivity of 192.7 S m^{-1} . LHHFs work as mechanically robust and stretchable capacitive iontronic strain/pressure sensors, showing a high sensitivity of 1.26 within 50% strain, and ultrahigh stability in cyclic tests with strain up to 200%

and pressure down to 500 Pa. Owing to their soft compliance with the human skin and high conductivity, LHHFs are utilized as epidermal electrodes to collect electrophysiological signals, such as ECG and EMG. During ECG monitoring for 48 h, high-fidelity signals can be continuously captured. We demonstrate a wearable LHHF-based multichannel sensing platform integrating LHHF iontronic capacitive sensors and LHHF electrodes at strategic body positions, connected via Bluetooth modules to PC/smartphone-based terminals. Long-term stable biomechanical and bioelectrical signals are simultaneously recorded for dynamic and comprehensive physiological monitoring. In sum, the LHHFs developed in this work possess a unique combinational attribute of high toughness, resilience, and conductivity, making them well-suited for soft bioelectronic sensors with high accuracy, stability, and durability, essential for monitoring of human physiological signals in practical wearable healthcare applications.

4. Experimental Section

The Experimental Section is available in the Supporting Information.

Supporting Information

Supporting Information is available from the Wiley Online Library or from the author.

Acknowledgements

This work was supported by the National Natural Science Foundation of China (Grant No. 52303321), A*STAR, RIE2025 Manufacturing, Trade and Connectivity (MTC) (M22K2c0081), the Natural Science Foundation of the Jiangsu Higher Education Institutions of China (Grant No. 23KJA430012), the National Natural Science Foundation of Jiangsu Province, China (Grant No. BK20230501), the PPM Institute of Functional Materials, Poly Plastic Masterbatch (Suzhou) Co., Ltd. (No. 2023004), the Opening Project of the Key Laboratory of Bionic Engineering (Ministry of Education), Jilin University (KF2023002), and the Soochow University Start-up Fund (NH11500323).

Conflict of Interest

The authors declare no conflict of interest.

Data Availability Statement

The data that support the findings of this study are available from the corresponding author upon reasonable request.

Keywords

conductive, hydrogel fiber, soft bioelectronics, strain-induced crystallization, tough yet resilient

Received: July 5, 2024
Revised: September 9, 2024
Published online: October 8, 2024

- [1] T. R. Ray, J. Choi, A. J. Bandothkar, S. Krishnan, P. Gutruf, L. Tian, R. Ghaffari, J. A. Rogers, *Chem Rev.* **2019**, *119*, 5461.
- [2] Y. Wang, H. Haick, S. Guo, C. Wang, S. Lee, T. Yokota, T. Someya, *Chem. Soc. Rev.* **2022**, *51*, 3759.
- [3] T. Someya, M. Amagai, *Nat. Biotechnol.* **2019**, *37*, 382.
- [4] H. C. Ates, P. Q. Nguyen, L. Gonzalez-Macia, E. Morales-Narváez, F. Güder, J. J. Collins, C. Dincer, *Nat. Rev. Mater.* **2022**, *7*, 887.
- [5] X.-Q. Wang, A.-Q. Xie, P. Cao, J. Yang, W. L. Ong, K.-Q. Zhang, G. W. Ho, *Adv. Mater.* **2024**, 2309952.
- [6] L. Hu, P. L. Chee, S. Sugiarto, Y. Yu, C. Shi, R. Yan, Z. Yao, X. Shi, J. Zhi, D. Kai, H.-D. Yu, W. Huang, *Adv. Mater.* **2023**, *35*, 2205326.
- [7] H. Yuk, B. Lu, X. Zhao, *Chem. Soc. Rev.* **2019**, *48*, 1642.
- [8] Z. Jiang, N. Chen, Z. Yi, J. Zhong, F. Zhang, S. Ji, R. Liao, Y. Wang, H. Li, Z. Liu, Y. Wang, T. Yokota, X. Liu, K. Fukuda, X. Chen, T. Someya, *Nat. Electron.* **2022**, *5*, 784.
- [9] S. Wang, L. Lei, Y. Tian, H. Ning, N. Hu, P. Wu, H. Jiang, L. Zhang, X. Luo, F. Liu, R. Zou, J. Wen, X. Wu, C. Xiang, J. Liu, *Mater. Horiz.* **2024**, *11*, 2131.
- [10] D. Myung, D. Waters, M. Wiseman, P. E. Duhamel, J. Noolandi, C. N. Ta, C. W. Frank, *Polym. Adv. Technol.* **2008**, *19*, 647.
- [11] J. P. Gong, *Soft Matter* **2010**, *6*, 2583.
- [12] A. K. Gaharwar, N. A. Peppas, A. Khademhosseini, *Biotechnol. Bioeng.* **2014**, *111*, 441.
- [13] X. Meng, Y. Qiao, C. Do, W. Bras, C. He, Y. Ke, T. P. Russell, D. Qiu, *Adv. Mater.* **2022**, *34*, 2108243.
- [14] L. Chen, Z. Jin, W. Feng, L. Sun, H. Xu, C. Wang, *Science* **2024**, *383*, 1455.
- [15] C. Liu, N. Morimoto, L. Jiang, S. Kawahara, T. Noritomi, H. Yokoyama, K. Mayumi, K. Ito, *Science* **2021**, *372*, 1078.
- [16] G. Nian, J. Kim, X. Bao, Z. Suo, *Adv. Mater.* **2022**, *34*, 2206577.
- [17] J. Kim, G. Zhang, M. Shi, Z. Suo, *Science* **2021**, *374*, 212.
- [18] W. Li, X. Wang, Z. Liu, X. Zou, Z. Shen, D. Liu, L. Li, Y. Guo, F. Yan, *Nat. Mater.* **2024**, *23*, 131.
- [19] D. Gao, K. Parida, P. S. Lee, *Adv. Funct. Mater.* **2020**, *30*, 1907184.
- [20] K. W. Cho, S.-H. Sunwoo, Y. J. Hong, J. H. Koo, J. H. Kim, S. Baik, T. Hyeon, D.-H. Kim, *Chem. Rev.* **2021**, *122*, 5068.
- [21] J. Wang, Q. Li, K. Li, X. Sun, Y. Wang, T. Zhuang, J. Yan, H. Wang, *Adv. Mater.* **2022**, *34*, 2109904.
- [22] T. Zhu, Y. Ni, G. M. Biesold, Y. Cheng, M. Ge, H. Li, J. Huang, Z. Lin, Y. Lai, *Chem. Soc. Rev.* **2023**, *52*, 473.
- [23] Q. Peng, J. Chen, T. Wang, X. Peng, J. Liu, X. Wang, J. Wang, H. Zeng, *InfoMat* **2020**, *2*, 843.
- [24] C. Wang, T. Yokota, T. Someya, *Chem. Rev.* **2021**, *121*, 2109.
- [25] S. Timoshenko, *J. Opt. Soc. Am.* **1925**, *11*, 233.
- [26] M. Kanik, S. Orguc, G. Varnavides, J. Kim, T. Benavides, D. Gonzalez, T. Akintilo, C. C. Tasan, A. P. Chandrakasan, Y. Fink, P. Anikeeva, *Science* **2019**, *365*, 145.
- [27] X. Wang, S. Zheng, J. Xiong, Z. Liu, Q. Li, W. Li, F. Yan, *Adv. Mater.* **2024**, 2313845.
- [28] T. Zhou, H. Yuk, F. Hu, J. Wu, F. Tian, H. Roh, Z. Shen, G. Gu, J. Xu, B. Lu, X. Zhao, *Nat. Mater.* **2023**, *22*, 895.
- [29] W. Wang, P. Guo, X. Liu, M. Chen, J. Li, Z. Hu, G. Li, Q. Chang, K. Shi, X. Wang, K. Lei, *Adv. Funct. Mater.* **2024**, 2316346.
- [30] X.-Q. Wang, K. H. Chan, W. Lu, T. Ding, S. W. L. Ng, Y. Cheng, T. Li, M. Hong, B. C. K. Tee, G. W. Ho, *Nat. Commun.* **2022**, *13*, 3369.
- [31] M. A. Higgs, R. Sass, *Acta Cryst* **1963**, *16*, 657.
- [32] F. Zuo, J. K. Keum, X. Chen, B. S. Hsiao, H. Chen, S.-Y. Lai, R. Wevers, J. Li, *Polymer* **2007**, *48*, 6867.
- [33] M. Lin, Z. Zheng, L. Yang, M. Luo, L. Fu, B. Lin, C. Xu, *Adv. Mater.* **2022**, *34*, 2107309.
- [34] R. Yang, A. Dutta, B. Li, N. Tiwari, W. Zhang, Z. Niu, Y. Gao, D. Erdely, X. Xin, T. Li, H. Cheng, *Nat. Commun.* **2023**, *14*, 2907.

- [35] L. Gao, M. Wang, W. Wang, H. Xu, Y. Wang, H. Zhao, K. Cao, D. Xu, L. Li, *Nano-Micro Lett.* **2021**, *13*, 140.
- [36] Y. Yuan, B. Liu, M. R. Adibeig, Q. Xue, C. Qin, Q. Sun, Y. Jin, M. Wang, C. Yang, *Adv. Mater.* **2024**, *36*, 2310429.
- [37] K. H. Kim, J. H. Kim, Y. J. Ko, H. E. Lee, *Soft Science* **2024**, *4*, 24.
- [38] Y. Xiong, J. Han, Y. Wang, Z. L. Wang, Q. Sun, *Research* **2022**, 9867378.
- [39] Y. Chang, L. Wang, R. Li, Z. Zhang, Q. Wang, J. Yang, C. F. Guo, T. Pan, *Adv. Mater.* **2021**, *33*, 2003464.
- [40] X. Zhang, Q. Fu, Y. Wang, H. Zhao, S. Hao, C. Ma, F. Xu, J. Yang, *Adv. Funct. Mater.* **2024**, *34*, 2307400.
- [41] A. Frutiger, J. T. Muth, D. M. Vogt, Y. Mengüç, A. Campo, A. D. Valentine, C. J. Walsh, J. A. Lewis, *Adv. Mater.* **2015**, *27*, 2440.
- [42] Y. Cheng, Y. Zhou, R. Wang, K. H. Chan, Y. Liu, T. Ding, X.-Q. Wang, T. Li, G. W. Ho, *ACS Nano* **2022**, *16*, 18608.
- [43] M. Fatkullin, V. Menzelintsev, A. Lipovka, E. Dogadina, E. Plotnikov, K. Brazovskiy, S. Li, L. Ma, C. Cheng, E. Porokhova, *ACS Sens.* **2024**, *9*, 1809.
- [44] A. Lipovka, M. Fatkullin, S. Shchadenko, I. Petrov, A. Chernova, E. Plotnikov, V. Menzelintsev, S. Li, L. Qiu, C. Cheng, R. D. Rodriguez, E. Sheremet, *ACS Appl. Mater. Interfaces* **2023**, *15*, 38946.
- [45] Q. Gao, F. Sun, Y. Li, L. Li, M. Liu, S. Wang, Y. Wang, T. Li, L. Liu, S. Feng, X. Wang, S. Agarwal, T. Zhang, *Nano-Micro Lett.* **2023**, *15*, 139.
- [46] S. Ji, C. Wan, T. Wang, Q. Li, G. Chen, J. Wang, Z. Liu, H. Yang, X. Liu, X. Chen, *Adv. Mater.* **2020**, *32*, 2001496.
- [47] M. Xia, J. Liu, B. J. Kim, Y. Gao, Y. Zhou, Y. Zhang, D. Cao, S. Zhao, Y. Li, J.-H. Ahn, *Adv. Sci.* **2024**, *11*, 2304871.
- [48] L. Zhang, K. S. Kumar, H. He, C. J. Cai, X. He, H. Gao, S. Yue, C. Li, R. C.-S. Seet, H. Ren, J. Ouyang, *Nat. Commun.* **2020**, *11*, 4683.